1   **Mie–Raman-Fluorescence lidar observations of aerosols during pollen season in the north**

2   **of France**

3   Igor Veselovskii[1], Qiaoyun Hu[2], Philippe Goloub[2], Thierry Podvin[2], Marie Choël[3], Nicolas

4   Visez[4], Mikhail Korenskiy[1]

5   *[1]Prokhorov General Physics Institute of the Russian Academy of Sciences, Moscow, Russia.*

6   *[2]Univ. Lille, CNRS, UMR 8518 - LOA - Laboratoire d'Optique Atmosphérique, Lille, 59000,*

7   *France*

8   *[3]Univ. Lille, CNRS, UMR 8516 - LASIR - Laboratoire de Spectrochimie Infrarouge et Raman,*

9   59000, Lille, France

10 *[4]Univ. Lille, CNRS, UMR 8522 - PC2A - Physicochimie des Processus de Combustion et de*

11 *l'Atmosphère, 59000, Lille, France*

13 **Abstract**

14 Multiwavelength Mie–Raman–fluorescence lidar of Lille University with the capability to

15 measure three aerosol backscattering, two extinction coefficients and three linear depolarization

16 ratios together with the fluorescence backscattering at 466 nm was used to characterize aerosols

17 during the pollen season in the north of France for the period March – June 2020. The results of

18 observations demonstrate that the presence of pollen grains in aerosol mixture leads to an

19 increase of the depolarization ratio. Moreover, the depolarization ratio exhibits a strong spectral

20 dependence increasing with wavelength, which is expected for the mixture containing fine

21 background aerosols with low depolarization and strongly depolarizing pollen grains. High

22 depolarization ratio correlates with the enhancement of the fluorescence backscattering,

23 corroborating the presence of pollen grains. Obtained results demonstrate that simultaneous

24 measurements of particle depolarization and fluorescence allows to separate dust, smoke

25 particles and aerosol mixtures containing the pollen grains.

27 **1. Introduction**

28   Pollen grains represent a significant fraction of primary biological particles emitted from the

29 biosphere into the atmosphere in certain seasons and locations (Fröhlich-Nowoisky et al., 2016).

30 There has been a growing interest in pollen study in recent years, because they can affect human

31 health by causing allergy-related diseases and contribute to the cloud formation by acting as

32 giant cloud condensation nuclei (CCN) (Diehl et al., 2001; Pope, 2010; D'Amato et al., 2014;
33 Steiner et al., 2015; Lake et al., 2017; Mack et al., 2020). To investigate the processes of pollen
34 transport and dispersion, the information about vertical distribution of pollen grains is needed,
35 and this information can be obtained from lidar measurements. Pollen grains are large irregularly
36 shaped particles of complicated morphology (Frenguelli, 2003), causing strong depolarization of
37 the backscattered laser radiation, which provides a basis for their identification. The first
38 profiling of pollen with depolarization lidar was reported by Sassen (2008, 2011). His
39 measurements over Alaska revealed that linear depolarization ratio of birch pollen plumes at 694
40 nm can exceed 30%. Further studies of pollen with elastic backscatter lidar at 532 nm were
41 reported by Noh et al. (2013 a,b) and by Sicard et al. (2016). Their measurements confirmed high
42 depolarization ratio of pollen grains (particle depolarization ratios as high as 43% were observed
43 for aerosol mixture containing *Platanus* and *Pinus* pollen). Moreover, pollen grains
44 backscattering demonstrated strong diurnal cycle, being highest near the noon. The use of
45 multiwavelength observations increases capability of lidar technique for aerosol characterization.
46 In recent studies of Bohlmann et al. (2019) and Shang et al., (2020) measurements performed
47 with Polly^{XT} lidar allowed to estimate mean values of the lidar ratios (about 45 sr and 55 sr at
48 355 and 532 nm respectively for birch pollen grains). The lidar measurement of pollen
49 depolarization ratio at 355 nm, 532 nm and 1565 nm was reported also in recent work of
50 Bohlmann et al. (2020), revealing strong decrease of depolarization ratio at 355 nm.

51 Atmospheric biological particles efficiently produce wideband fluorescence emission,
52 when being exposed to UV radiation (Pohlker et al., 2012; Pan, 2015; Miyakawa et al., 2015),
53 which offers an opportunity for monitoring them with fluorescence lidars. Nowadays, lidar
54 spectrometers based on multianode photomultipliers allow a simultaneous detection of
55 fluorescence backscattering in 32 spectral bins (Sugimoto et al., 2012; Reichardt et al., 2014,
56 2017; Saito et al., 2018; Richardson et all, 2019). In particular, such lidar spectrometer was used
57 in recent work of Saito et al. (2018) for remote measurement of the fluorescence spectrum of
58 atmospheric pollen grains. The results demonstrate that, for 355 nm stimulating wavelength, the
59 fluorescence spectra of different pollen grains have maxima in the 400–600 nm range and the
60 intensity peak at around 460 nm.

61 To achieve the highest sensitivity of fluorescence detection, in many tasks it is preferable
62 to use a single channel monitoring, where a part of the fluorescence spectrum is selected with a

63 wideband interference filter (Immler et al, 2005; Rao et al., 2018; Li et al., 2019). In our recent

64 publication (Veselovskii et al., 2020a) we reported the results obtained from a modified Mie–

65 Raman lidar system in Laboratoire d'optique Atmosphérique with one additional fluorescence

66 channel at 466 nm. Such an approach has proved high sensitivity, allowing to detect fluorescence

67 signals from weak aerosol layers and to calculate the fluorescence backscattering coefficient

68 from the ratio of fluorescence and nitrogen Raman backscatters, thus making it potentially

69 attractive for pollen monitoring.

70   In the present research we combine capability of multiwavelength Mie–Raman lidar for

71 providing three backscattering, two aerosol extinction coefficients and linear depolarization ratio

72 at three wavelengths with single channel fluorescence measurements for characterization of

73 aerosol mixtures containing pollen grains. The measurements reported were performed during

74 March–June 2020 period at the Lille Atmospheric Observation Platform (https://www-loa.univ-

75 lille1.fr/observations/plateformes.html?p=apropos) hosted by Laboratoire d'Optique

76 Atmospherique, University of Lille, Hauts-de-France region.

77

78 **2. Instrumentation**

79 **2.1 Mie-Raman-Fluorescence lidar**

80   The measurements were performed using LILAS (LIlle Lidar AtmosphereS) system – a

81 multiwavelength Mie-Raman lidar, based on a tripled Nd:YAG laser with a 20 Hz repetition rate

82 and pulse energy of 70 mJ at 355 nm. The backscattered light is collected by a 40 cm aperture

83 Newtonian telescope. The full geometrical overlap of the laser beam and the telescope FOV is

84 achieved at approximately 1000 m and to obtain the information about particles at lower altitudes,

85 part of the measurements were performed at an angle of 30 degrees to the horizon. No overlap

86 correction of lidar signals was performed. The system is designed for a simultaneous detection of

87 elastic and Raman backscattering, allowing the so called $3\beta+2\alpha+3\delta$ data configuration, including

88 three particle backscattering (β_{355}, β_{532}, β_{1064}), two extinction (α_{355}, α_{532}) coefficients along with

89 three particle depolarization ratios (δ_{355}, δ_{532}, δ_{1064}). The particle depolarization ratio δ,

90 determined as a ratio of cross- and co-polarized components of the particle backscattering

91 coefficient, was calculated and calibrated the same way as described in Freudenthaler et al.

92 (2009). The description of the system can be found in the recent publication of Hu et al., (2019).

To perform fluorescence lidar measurements, the water vapor Raman channel at 408 nm was replaced by a fluorescence channel, whose spectrum is captured by a wideband filter centered at 466 nm and of 44 nm width (Veselovskii et al., 2020a). The fluorescence measurements were performed during night time only. The aerosol extinction and backscattering coefficients at 355 and 532 nm were calculated from Mie-Raman observations (Ansmann et al., 1992), while β_{1064} was derived by the Klett method (Klett, 1985). The fluorescence backscattering coefficient β_F is calculated from the ratio of fluorescence and nitrogen Raman backscattering, as described in Veselovskii et al. (2020a). This approach allows to evaluate the absolute values of β_F, if the relative sensitivity of the channels is calibrated and the nitrogen Raman scattering cross section is known. Corresponding uncertainty we estimate to be below 50%. Parameters of detectors were not changed during the campaign, so uncertainty of relative variations of β_F was significantly lower and was determined by the statistical errors of fluorescence measurements.

To characterize the efficiency of the fluorescence in respect to elastic scattering, the fluorescence capacity

$$G_F = \frac{\beta_F}{\beta_{532}} \tag{1}$$

is also used. This parameter depends on the relative humidity (RH), so information about RH is important for data analysis. Radiosonde measurements are used to monitor water vapor, as the water vapor channel is replaced by the fluorescence channel in current lidar configuration. The closest available radiosonde data are from Herstmonceux (UK) and Beauvecchain (Belgium) stations, located 160 km and 80 km away from the observation site respectively. These radiosonde data are not collocated with the lidar measurements, so only qualitative analysis of humidification effects was possible.

2.2 Pollen in situ sampling

Airborne pollen grains and spores were collected by a Hirst-type volumetric sampler (VPPS 2000, Lanzoni s.r.l). The pollen sampler was located on the campus of the University of Lille (France) on the rooftop of a 20-m-high building where the lidar instrument was operated. Ambient air was sampled at 10 L.min^{-1} flow rate, allowing the impaction of pollen and spores on an adhesive strip mounted on a rotating clockwork-driven drum. The impaction surface moves at

123   2 mm.h^{-1} behind the entrance slit, allowing a temporal resolution of 2 hours. The adhesive strip

124   was substituted every 7 days after a full rotation of the drum, which is splitted into 7 parts, each

125   corresponding to a day of monitoring. And then they are fixed on a microscope glass slide with

126   gelatin and fuchsine dye. Pollen taxa were identified by light microscopy on the basis of their

127   characteristic shape and size. Airborne pollen concentrations were expressed as a daily and dual

128   hourly number of pollen grains per cubic meter of air.

129   Fig.1 shows the most abundant pollen taxa for the period from March to June 2020 in

130   Lille. These include: *Betula* (54.8% of total pollen taxa over the period), *Fraxinus* (8.2%),

131   *Quercus* (5.8%), *Urticaceae* (4.6%), *Salix* (4.5%) and *Cupressaceae* (4.1%). The same figure

132   shows also the fluorescence backscattering β_F measured by lidar. The results presented are

133   obtained by averaging all available data during the night and the maximal values in 500 – 1000

134   m height range are shown. The highest fluorescence was observed in the end of March, when ash

135   (*Fraxinus*) is the main pollinator. The period of intense birch (*Betula*) pollination (3-15 April

136   2020) correlates also with high β_F. Strong fluorescence observed for 5-10 May and 28 May–2

137   June periods, can be due to grass (*Poaceae*) pollen contribution. By the end of June, β_F decreases

138   and becomes comparable with fluorescence backscattering of background aerosol. From Fig.1,

139   we can conclude that there is no direct correlation between in situ and fluorescence lidar

140   measurements, thus pollen observed in the boundary layer by the lidar are probably transported

141   from other regions. Comparing lidar and in situ observations, we should also keep in mind, that

142   maximum of pollen emission occurs near the noon, while lidar measurements were performed in

143   the night.

144

145   **3. Discrimination of pollen from other types of aerosol**

146   *3.1. Specific features of pollen containing aerosol mixture*

147   In contrast to the observations performed over Alaska (Sassen, 2008, 2011) or in Kuopio,

148   Finland (Bohlmann et al., 2019), where pollen concentration was high due to boreal forests

149   surrounding, the pollen loading in the north of France is significantly lower. Long-term lidar and

150   sun photometer observations performed at Lille University demonstrate that local aerosol is

151   mainly of continental type, with predominance of the fine mode particles and low depolarization

152   ratio. The emission of large pollen grains, should lead to strong spectral dependence of the

153   depolarization ratio, because the backscattering at 1064 is less sensitive to the fine background

particles than at shorter wavelengths, thus particle depolarization ratio at 1064 nm (δ_{1064}) should

be more sensitive to the presence of pollen grains, compared to δ_{355} and δ_{532}. The particle

depolarization ratio δ of the mixture, containing background aerosol (*b*) and pollen (*p*), with

corresponding depolarization ratios δ^b and δ^p, can be calculated as:

$$\delta = \frac{\left(\dfrac{\delta^p}{1+\delta^p}\right)\beta^p + \left(\dfrac{\delta^b}{1+\delta^b}\right)\beta^b}{\dfrac{\beta^p}{1+\delta^p} + \dfrac{\beta^b}{1+\delta^b}} \qquad (2)$$

Here total backscattering $\beta = \beta^b + \beta^p$.

To estimate the dependence of depolarization of the aerosol mixture on the contribution

of pollen to the backscattering coefficient $\dfrac{\beta^p_{532}}{\beta_{532}}$ at 532 nm, a simplified simulation was

performed. Assuming that the depolarization ratios of pollen and background aerosol are

spectrally independent and that δ^p=30% while δ^b=3%, the mixture depolarization ratios δ_{355}, δ_{532},

δ_{1064} were calculated as a function of $\dfrac{\beta^p_{532}}{\beta_{532}}$ using expression (2). For pollen the backscattering

Angstrom exponents (BAE) $A^{\beta}_{355/532} = A^{\beta}_{532/1064} = 0$ were used. The backscattering Angstrom

exponents of background aerosol are assumed to be the same for both wavelength pairs

($A^{\beta}_{355/532} = A^{\beta}_{532/1064}$), and computations were performed for the values of BAE A^{β}=1.0, 1.5, 2.0.

Results of simulation are shown in Fig.2. For low pollen contribution the depolarization ratio

δ_{1064} increases faster with $\dfrac{\beta^p_{532}}{\beta_{532}}$, comparing to δ_{532} and δ_{355}, and the slop of this increase depends

on the BAE value. Spectral properties of the real mixture can be more complicated, due to

possible spectral dependence of both δ^p and δ^b. Information on laboratory measured spectral

dependence of depolarization ratios of pollen is rare. Cao et al. (2010) measured the linear

depolarization ratio of several types of pollen in a chamber at 355, 532 and 1064 nm

wavelengths. The results demonstrate strong variation of spectral dependence for different taxa,

and for most of the samples δ_{532} exceeded both δ_{355} and δ_{1064}. In particular, for birch pollen,

depolarization ratios at 355 nm, 532 nm and 1064 nm are of 8%, 33% and 28%. Using the

depolarization ratios from Cao et al. (2010) in analysis, we should also keep in mind that

178 measurements in the chamber were performed at low RH, and depolarization ratios at higher RH
179 may be different.

180 The Angstrom exponents $A^{\beta}_{355/532}$ and $A^{\beta}_{532/1064}$ depend on the particle size and the
181 refractive index in different way (Veselovskii et al., 2015), so their values can be different. Thus
182 spectral dependence of depolarization ratio of aerosol - pollen mixture will differ from simplified
183 modeling shown in Fig.2. However, for moderate contribution of pollen to the total
184 backscattering ($\frac{\beta^{p}_{532}}{\beta_{532}}$ below ≈0.5), the depolarization ratio at 1064 nm should be higher than that
185 at shorter wavelengths. Hence, increase of the particle depolarization ratio with wavelength can
186 be an indication of the presence of large, irregularly-shaped pollen grains in aerosol mixture.

187 The presence of pollen should lead also to the decrease of the extinction and
188 backscattering Angstrom exponents. Extinction Angstrom exponent (EAE) depends mainly on
189 particle size, while BAE is sensitive also to the particle complex refractive index and shape, thus
190 the measured profiles of EAE and BAE can present significant difference (Veselovskii et al.,
191 2015, 2020b). In our study we analyze the EAE and BAE for the wavelength pair 355/532 nm
192 ($A^{\alpha}_{355/532}$ and $A^{\beta}_{355/532}$) only, because the extinction and backscattering coefficient involved are
193 calculated from Mie–Raman observations.

194 When analyzing Mie-Raman-fluorescence lidar measurements of pollen containing
195 aerosol mixtures, the numerous factors should be taken into account. These factors include the
196 fluorescence of background aerosol and other non-pollen aerosols that have strong fluorescence
197 capacity, for example, smoke particles. Dust particles can contribute to the increase of
198 depolarization ratio and, finally, the hygroscopic growth can modify the particle parameters. All
199 these factors will be considered in following sections.

200

201 *3.2. Characteristics of background aerosol over observation site*.

202 Long-term observations in Lille University demonstrate that aerosol over the observation
203 site is mainly of continental type with predominance of the fine mode particles. Typical vertical
204 profiles of the background aerosol parameters, observed on 3 June 2020, are given in Fig.3,
205 showing aerosol elastic and fluorescence backscattering coefficients, lidar ratios, Angstrom
206 exponents and depolarization ratios at three wavelengths. The RH from Beauvechain (Belgium)
207 radiosonde observations, was below 50% in the height range considered. Particle depolarization

208   ratios at all three wavelengths are below 7%, indicating that contribution of pollen to the total

209   backscattering was low. This agrees with the low values of pollen concentration provided by in

210   situ measurements (Fig.1). The lidar ratios at both wavelengths (S_{355}, S_{532}) are close, varying in

211   the 50-60 sr range, and the fluorescence capacity G_F is below 0.35×10^{-4}. The EAE and BAE

212   ($A^{\alpha}_{355/532}$, $A^{\beta}_{355/532}$) are in the 1.5–2.0 range. The presence of pollen should lead to a deviation of

213   the particle intensive parameters, such as the fluorescence capacity, depolarization ratio, EAE

214   and BAE, from the typical values of background aerosol.

215

216   *3.3 Identification of the smoke particles*

217   During the observation period the smoke elevated layers transported over Atlantic were

218   frequently detected. Smoke particles, are characterized by high fluorescence cross section

219   (Reichardt et al., 2017; Veselovskii et al., 2020a) and can interfere pollen fluorescence

220   measurements. The temporal evolution of the range corrected lidar signal, volume depolarization

221   ratio at 1064 nm and fluorescence backscattering for the smoke episode on the night 23 – 24

222   June 2020 are shown in Fig.4. During the night the smoke layer with low depolarization and high

223   fluorescence is observed at approximately 5000 m height. Back trajectories (not shown) indicate

224   that the layer is transported from Canada. Vertical profiles of the particle parameters for this

225   episode are shown in Fig.5. The lidar ratio is about 50 sr at 355 nm, while the lidar ratio at 532

226   nm increases within the smoke layer from 60 sr to 80 sr. This increase of S_{532} occurs

227   simultaneously with decrease of $A^{\alpha}_{355/532}$ from 1.5 to 0.75, indicating that the particle size inside

228   the layer growths with height. Higher values of S_{532} in respect to S_{355} are typical characteristics

229   for the aged smoke (e.g. Müller et al., 2005; Nicolae et al., 2013; Hu et al., 2019). The

230   depolarization ratio decreases with wavelength from δ_{355}=10% to δ_{1064}=1.5%. Strong spectral

231   dependence of depolarization ratio and, in particular, low values of δ_{1064}, are the features,

232   allowing to identify the smoke layers. We should recall also, that increase of the particle

233   depolarization ratio at 355 nm is more typical for the aged smoke layers in the high troposphere

234   (Haarig et al., 2018), though we observed this increase at lower altitudes over Lille during smoke

235   episodes in Summer – Autumn 2020.

236   The extinction Angstrom exponent $A^{\alpha}_{355/532}$ in the center of layer is about 0.75, while

237     $A^{\beta}_{355/532}$ is about 1.9 and shows no significant variation through the layer. High values of $A^{\beta}_{355/532}$

238   compared to $A^{\alpha}_{355/532}$ is another feature that will be used for aged smoke discrimination. Smoke

239   fluorescence capacity is high, reaching up to $G_F=5*10^{-4}$ for the period of observations, and this is

240   one more feature, allowing to separate smoke from other types of aerosol.

241

242   *3.4 Identification of the dust particles*

243   Presence of dust particles and pollen in the fine background aerosol leads to some

244   common characteristics in the lidar data, such as the decrease Angstrom exponents and increase

245   of depolarization ratios. However, pollen and dust can be separated by the fluorescence capacity.

246   The vertical profiles of particle parameters during dust episode on 27 May are shown in Fig.6.

247   The dust containing layer extends from 2000 m to 7000 m and the particle depolarization ratios

248   δ_{1064} and δ_{532} in this layer are close to 20%. These values are lower than depolarization of pure

249   dust. For example, Freudenthaler et al. (2009) for pure dust provide the values of 27% and 31%

250   at 1064 nm and 532 nm wavelengths respectively, thus in our case transported dust particles may

251   be mixed with local aerosols. The particle depolarization at 355 nm is not shown in the figure,

252   because the scattering ratio in the dust layer was too low to compute δ_{355} reliably. The

253   fluorescence capacity of particles in the dust layer is about 0.1×10^{-4} at 4000 m, which is factor 50

254   lower than G_F of the smoke in Fig.5. There is also a weak aerosol layer at 1600 m with β_{532}

255   about 0.035 $Mm^{-1}sr^{-1}$. The fluorescence capacity in this layer is high ($G_F\approx2.0*10^{-4}$), suggesting

256   that this layer may contain smoke or pollen particles.

257

258   *3.5 Impact of particle hygroscopic growth*

259   The vertical variation of observed aerosol properties may be a result of particle water

260   uptake, which should be separated from the features related to pollen presence. Fig.7 shows the

261   profiles of the particle parameters for the episode on 15 June 2020, when the aerosol hygroscopic

262   growth could take place. In the height range 900–1500 m the fluorescence backscattering β_F is

263   stable, while the elastic backscattering β_{532} increases by a factor 3. Radiosonde measurements in

264   Herstmonceux (UK) in this height range demonstrate an increase of RH from about 75% to 85%,

265   while lidar measured extinction and backscattering Angstrom exponents decrease from 1.5 to 1.3,

266   corroborating the presence the particle hygroscopic growth. The depolarization ratio δ_{1064} at low

267   altitudes exceeds δ_{355} and δ_{532}, which can be an indication of pollen presence. This is supported

268   by significant fluorescence capacity ($G_F=0.9\times10^{-4}$ at 750 m).

269   The number of fluorescent particles in the 900–1500 m range, does not present significant
270   changes (β_F is stable), so observed vertical variations, i.e. the decrease of depolarization ratios at
271   all three wavelengths and the increase of lidar ratios S_{355} and S_{532} from 50 sr to 65 sr, are
272   probably the result of water uptake by the particles. Water uptake does not change the number of
273   fluorescent molecules, however the fluorescence capacity decreases in the process of the
274   hygroscopic growth, so G_F can be a representative parameter of aerosol types only at the
275   condition of low RH.
276
4. Results of lidar measurements in the presence of pollen

278   During March–June 2020, we had numerous measurement cases demonstrating the
279   features in the profiles of the particle parameters, that can be attributed to pollen. For
280   representative cases we have chosen observations with high depolarization ratio and high
281   fluorescence backscattering. The same time, we omitted the days with high relative humidity, to
282   minimize the impact of the hygroscopic growth effects. Below we consider several measurement
283   cases representing different scenarios, in particular, the episodes when pollen concentration
284   decreases with height (30-31 May, 1-2 June) and the episodes when pollen grains are well mixed
285   inside the boundary layer (27-28 March and 21 April).
286
4.1. 30-31 May and 1-2 June 2020 observations

288   The results of lidar measurements during the campaign in many episodes can be
289   interpreted as decrease of pollen concentration with height. Vertical profiles of the main particle
290   parameters for two representative cases in the nights of 30-31 May and 1-2 June 2020, are shown
291   in Fig.8. The atmospheric conditions for these nights were stable so the profiles presented are
292   averaged over approximately five hours interval. The HYSPLIT back trajectory analysis (Stein et
293   al., 2015) demonstrates that in 1000--2000 m height range the air masses were transported from
294   the Northern Europe. At the ground level, the grass could be the main pollen contributor for this
295   period, as shown in Fig 1. On 31 May (at 00:00 UTC) the RH measured by the radiosonde in
296   Herstmonceux (UK) was about 40% at 500 m and it increased up to 70% at 2000 m. On 2 June
297   the RH increased from approximately 40% to 60% in the same height range. For both nights the
298   fluorescence backscattering decreases with height, indicating the decrease of the concentration of
299   fluorescent particles (presumably pollen). This decrease of β_F correlates with decrement of the

300 depolarization ratio at all three wavelengths. Particle depolarization δ_{1064} is the highest (about 15%

301 at 750 m), while δ_{355} and δ_{532} are significantly lower. Such spectral dependence of depolarization

302 ratio can be partly due to the contribution of the background aerosol, as follows from model

303 calculation in Fig.2. The lidar ratios are available above 1250 m and for both cases, S_{355} and S_{532}

304 increase with height. It indicates that the lidar ratios of pollen in the two considered cases can be

305 quite low: below 40 sr at 355 nm and below 30 sr at 532 nm, considering that pollen

306 concentration decreases with height, which is inferred from the features of depolarization ratio

307 and fluorescence backscattering

308 The EAE for both nights varied in 1.75 - 2.0 range and did not show significant changes

309 with height. The BAE is lower (about 1.5 at 1000 m) and for both nights it shows some increase

310 in 1250–2250 m range. The BAE, in contrast to EAE, depends strongly on the particle refractive

311 index and shape, thus it may demonstrate higher sensitivity to the changes in aerosol mixture

312 composition. Recall that backscattering and extinction Angstrom exponents are related as:

313
$$A^{\beta}_{355/532} = A^{\alpha}_{355/532} + \frac{\ln(S_{532}/S_{355})}{\ln(355/532)} \qquad (3)$$

314 Thus for $S_{355} > S_{532}$, which has been observed during pollen episodes, the $A^{\beta}_{355/532}$ is lower than

315 $A^{\alpha}_{355/532}$. This is in contrast with smoke episodes, where $S_{355} < S_{532}$ and $A^{\beta}_{355/532} > A^{\alpha}_{355/532}$ (Fig.5).

316 If the depolarization ratios of pollen δ^{p} and background aerosol δ^{b} are known, the pollen

317 backscattering coefficient β^{p} can be calculated. Such approach is widely used for the separation

318 of contributions of dust and smoke particles (Sugimoto and Lee, 2006; Tesche et al., 2009) and

319 the same technique was applied to separate pollen and background aerosol (Noh et al. 2013a;

320 Sicard et al., 2016; Shang et al., 2020). For height independent depolarization ratios of pollen

321 and background aerosol the pollen backscattering coefficient can be calculated as suggested by

322 Tesche et al. (2009):

323
$$\beta^{p} = \beta \frac{(\delta - \delta^{b})}{(\delta^{p} - \delta^{b})} \frac{(1 + \delta^{p})}{(1 + \delta)} \quad , \qquad (4)$$

324 Here β and δ are backscattering coefficient and particle depolarization ratio of the mixture. The

325 profiles of β^{p}_{532} and the relative contribution $\dfrac{\beta^{p}_{532}}{\beta_{532}}$ are shown in Fig.8(b,e). Computations were

326 performed in assumption of height independent $\delta^{p}_{532} = 30\%$. For background aerosol, the values

327    $\delta_{532}^{b} = 3\%$ for 30-31 May and $\delta_{532}^{b} = 5\%$ for 1-2 June were used. On $30 - 31$ May contribution of

328   pollen $\dfrac{\beta_{532}^{p}}{\beta_{532}}$ at 750 m is estimated as 30%.

329   The profiles of β_F and β_{532}^{p} in Fig.8(b, e) behave similarly, decreasing with height. Above

330   2000 m the decrease of β_F slows down due to the fluorescence of background aerosol. The

331   profiles of the fluorescence capacity G_F and relative contribution $\dfrac{\beta_{532}^{p}}{\beta_{532}}$ also demonstrate a good

332   correlation. Thus both depolarization and fluorescence techniques lead to the same conclusion:

333   pollen concentration in the boundary layer for the considered episodes decreases with height.

334

335   ***4.2. 27 – 28 March and 21 April 2020 observations.***

336   According to the in-situ pollen sampling at rooftop level, the maximal pollen content was

337   detected during birch pollination period on 4–20 April. However, the maximal fluorescence

338   backscattering of lidar data was observed in the end of March, when sampling shows an increase

339   of ash (*fraxinus*) pollen emission. The temporal evolution of range corrected lidar signal, volume

340   depolarization ratio at 1064 nm and fluorescence backscattering on 27-28 March night is shown

341   in Fig.9. The main part of the aerosol is localized below 2000 m. The back trajectory analysis

342   demonstrates the air masses in this episode were transported from the East Europe. In contrast

343   with Fig.8, where fluorescence decreases with height, on 27 -28 March the fluorescent particles

344   are rather well mixed inside the PBL (planetary boundary layer). The fluorescence

345   backscattering is high, exceeding 2.5×10^{-4} Mm^{-1}sr^{-1} and the volume depolarization at 1064 nm is

346   about 15%. The vertical profiles of the particle parameters, averaged for period 19:20 – 04:30

347   UTC, are shown in Fig.10. In spite of temporal variations of the lidar signal and the fluorescence

348   backscattering inside the PBL (Fig.9), the averaged over night profiles of particle parameters are

349   representative. Radiosonde measurements (at both Beauvecchain and Herstmonceux sites) show

350   that RH gradually increased with height from approximately 40% to 70% in 500–1750 m range.

351   The depolarization ratios δ_{532} and δ_{1064} inside the PBL are close, which is in contrast with results

352   in Fig.8, where δ_{1064} exceeds δ_{532}. This difference can be due to the different types of pollen

353   occured, which is probably grass in Fig.8 and birch in Fig.10. Besides, the BAE in Fig.10 is

354
355

356 Both the fluorescence backscattering and depolarization ratios do not demonstrate strong

357 variations inside the 600–1500 m range. The maximum of fluorescence capacity exceeds 1.2×10^{-4}

358 , which is significantly higher than G_F for background aerosol in Fig.3. The profiles of G_F and

359 $\dfrac{\beta^p_{532}}{\beta_{532}}$ behave reasonably similar, the slight decrease of $\dfrac{\beta^p_{532}}{\beta_{532}}$ with height in respect to G_F can be

360 due to dependence of depolarization ratio of pollen on RH.

361 Agreements between results obtained from depolarization and fluorescence techniques in

362 Fig.8,10, corroborates the suggestion that the observed fluorescence is mainly due to the

363 presence of pollen. However, in some episodes the particles with high fluorescence cross section,

364 other than pollen, could interfere. In particular, such interference occurred in 20-23 April 2020

365 period. Fig.11 shows the vertical profiles of particle parameters measured on 21 April. The

366 depolarization ratio δ_{1064}=22% at 750 m was one of the highest during campaign. The RH was

367 low, increasing from 30% to 45% in 800–1500 m range, according to Herstmonceux radio

368 sounding. The back trajectory analysis demonstrates, that below 1500 m the air masses are

369 transported from Spain, while at 2000 m the transportation is from the Northern Europe.

370 Fluorescence backscattering is stable in 500–1500 m range and the fluorescence capacity

371 at 1000 m is about 1.5×10^{-4}, which is a typical value for the pollen. However, above 1250 m G_F

372 starts to rise, reaching the value of 2.5×10^{-4} at 1750 m. Such high G_F is more typical for the

373 smoke particles. Depolarization ratio δ_{355} is about 15%, and this is higher than corresponding

374 values shown in Fig.8, 10, which again may corroborate the presence of smoke particles. We

375 should recall, that smoke particles are small, so, in contrast to pollen, their presence influences

376 δ_{355} stronger than δ_{1064}. The enhanced values of δ_{355} and G_F were observed during 20-23 April

377 period, indicating to the possible presence of the biomass burning particles in the aerosol mixture.

378

4.3. Separation of pollen and smoke layers

380 During the campaign we observed narrow layers with strong fluorescence. Two examples

381 of such observations, in the nights 13-14 April and 16-27 May 2020, are shown in Fig.12. The

382 white arrows on this figure point to the fluorescent layers. On 13 April, a weak aerosol layer

383 ($\beta_{532}\approx0.6$ Mm^{-1}sr^{-1} for 23:00 – 00:00 UTC) is observed at the top of the PBL. This layer

384 demonstrates volume depolarization ratios about 10% and high fluorescence backscattering. On

385 26-27 May a weak layer with high fluorescence backscattering occurs between 3 km and 4 km.

386 However, in contrast with the first case, it has low depolarization ratio, so the layers may have

387 different nature. Fig.13 shows the vertical profiles of the particle parameters for these two cases.

388 On 13-14 April the fluorescence backscattering below 1000 m is stable, while β_{532} rises, which

389 can be the result of the particle water uptake. Above 1000 m, the depolarization ratio δ_{1064}

390 increases up to 8%. Results in Fig.13a are averaged over 21:15–00:40 UTC temporal interval,

391 but peak values of δ_{1064} between 23:00 and 00:00 exceeded 12%. Fluorescence backscattering

392 increases simultaneously with the depolarization. The aerosol backscattering coefficient of

393 fluorescent layer is too low for a reliable calculation of δ_{355} and δ_{532}, so only the profile of δ_{1064}

394 is provided.

395   On 26-27 May the backscattering coefficient of the fluorescent layer at 3400 m is lower

396 than in Fig.13a ($\beta_{532} \approx 0.14$ Mm^{-1}sr^{-1}), so the depolarization ratio δ_{1064} can be calculated only in

397 the center of the layer and it is about 2%, which is significantly lower than that on 13-14 April.

398 However, the fluorescence capacity on 26-27 May is up to 3.5×10^{-4}, which is typical for smoke.

399 Thus, we can conclude that the fluorescent layer on 26-27 May contains the smoke particles, due

400 to high G_F and low δ_{1064}. On 13-14 April, the fluorescence capacity is significantly lower (about

401 0.9×10^{-4}) and depolarization ratio δ_{1064} exceeds 10%, which is more typical for pollen. Due to

402 low backscattering coefficients of the fluorescent layers in Fig.12, we are not able to provide a

403 complete set of intensive parameters, such as Angstrom exponents and particle depolarization

404 ratios at three wavelengths. However, based on the obtained fluorescence capacities and δ_{1064}

405 values, we conclude that the fluorescent layers probably contain pollen grain in Fig.12a, and

406 smoke particles in Fig.12b.

407

408   ***4.4 Aerosol classification based on polarization and fluorescence measurements.***

409   Table 1 summarizes the results in the campaign, showing the aerosol parameters, such as

410 particle depolarization and lidar ratios, extinction Angstrom exponent, fluorescence

411 backscattering and capacity for several days in March–June 2020 observations period, when the

412 contribution of pollen to the total particle backscattering was significant. All available night

413 observations were averaged and results are given for heights with the highest particle

414 depolarization. Lidar ratios varied approximately in 40-70 sr range, wherein normally S_{355} is

415 greater than S_{532}. It must be emphasized that pollen lidar ratios may differ for different taxa and
416 that the observed lidar ratios are not attributed to pure pollen, but to the aerosol–pollen mixture,
417 so the values provided are influenced by the properties of background aerosol. Moreover, the
418 shape of pollen grains depends on RH, (Heidemarie et al., 2018), which may also lead to the
419 variation of pollen lidar ratios. In most of the cases, the depolarization ratio presents strong
420 spectral dependence and increases with wavelength. This spectral dependence is probably the
421 result of mixing of strongly depolarizing pollen grains with fine background aerosol. The
422 maximal value of observed fluorescence capacity of pollen-aerosol mixture is 1.6×10^{-4}, which is
423 significantly higher than that of background aerosol, but lower than fluorescence capacity of
424 smoke.

425   The simultaneous observations of depolarization ratio and fluorescence capacity for
426 different types of aerosol are summarized by Fig.14. On this plot, particle depolarization δ_{532} is
427 plotted versus G_F. The diagram allows to separate four types of the particles: (i) dust particles –
428 high δ_{532} and low G_F; (ii) pollen – high δ_{532} and high G_F; (iii) smoke – low δ_{532} and high G_F; (iiii)
429 background aerosol (continental type) - low δ_{532} and low G_F. Points corresponding to the pollen
430 mixture provide extended pattern, because parameters depend on the concentration of pollen in
431 the aerosol mixture. The dust measurements are also scattered, because dust over the
432 instrumentation site is long transported and mixed with local aerosol. Minimum G_F for dust is
433 about 0.1×10^{-4} while for smoke maximal G_F is about factor 50 higher. The fluorescence capacity
434 depends on the relative humidity, so strong scattering of measurement points can be partly also
435 due to RH variations. Maximal values of G_F for pollen mixture were about 1.5×10^{-4}, and the
436 corresponding depolarization ratios δ_{532} are about 18%. Thus, assuming that depolarization ratio
437 of pure pollen is 30%, we can expect G_F for pure pollen to be about 2.5×10^{-4}, which is
438 comparable with values for smoke.

439

440   **Conclusion**

441   We analyzed the measurements from a multiwavelength Mie-Raman-fluorescence lidar
442 during March–June 2020 in the north of France, to reveal the features that can be attributed to
443 pollen grains. The lidar system allowed to measure depolarization ratios at three wavelengths,
444 simultaneously with the fluorescence backscattering at 466 nm. In numerous episodes during the
445 campaign, high values of the particle depolarization ratio at 1064 nm, exceeding 15%, were

446 observed. Moreover, depolarization ratio had strong spectral dependence, being the highest at
447 1064 nm and lowest at 355 nm, which is expectable for big particles of irregular shape mixed
448 with fine, low depolarizing background aerosol. The increase of particle depolarization
449 correlated with enhancement of the fluorescence backscattering corroborating that in these
450 episodes we observed aerosol mixtures containing pollen.

451   The lidar ratios of aerosol–pollen mixtures observed during campaign varied in a wide
452 range. At low altitudes, where particle presented strong depolarization and fluorescence, in many
453 cases we observed lidar ratios below 40 sr at both wavelengths. However, we had also cases
454 when the lidar ratios at both wavelengths were in 50–60 sr range. Thus, at the moment we are not
455 capable to specify lidar ratios for pure pollen and additional measurement campaigns in the
456 locations with high pollen content are strongly desirable.

457   Obtained results demonstrate, that simultaneous measurements of particle depolarization
458 and fluorescence allows to separate dust, smoke particles and pollen grains. Moreover, the
459 fluorescence measurements provide additional information that can be used in aerosol
460 classification schemes. However, further studies are needed to make this technique applicable for
461 the quantitative pollen characterization. In the data analysis it is important to account for the
462 process of water uptake by the particles, because hygroscopic growth increases backscattering of
463 background aerosol and influences the pollen grain shape. In the presented lidar configuration,
464 the water vapor channel was absent and radiosonde RH data were not collocated with lidar,
465 which prevented us from performing a quantitative analysis of the hygroscopic effects. Since
466 December 2020, we recovered the water vapor channel in upgraded configuration of the lidar.
467 Moreover, we added one more fluorescence channel centered at 549 nm, which will be used in
468 the next pollen campaign in 2021. This additional channel should improve discrimination of the
469 pollen from other aerosols. In coming campaign we will try to correlate our results with pollen
470 concentration at different location in Europe by using the transport model, e.g. SILAM (System
471 for Integrated modeLling of Atmospheric coMposition) (Sofiev et al, 2013, 2015). The use of
472 this model should help in identification of pollen type in our observations.

473

474 **Acknowledgement**
475 We acknowledge funding from the CaPPA project funded by the ANR through the PIA under
476 contract ANR-11-LABX-0005-01, the "Hauts de France" Regional Council and the European

477 Regional Development Fund (ERDF). The "Réseau National de Surveillance Aérobiologique"
478 (RNSA) and the "Association pour la Prévention de la Pollution Atmosphérique" (APPA) are
479 gratefully acknowledged for providing Hirst-collected pollen grains identification and for
480 assistance with the pollen data handling. Development of lidar retrieval algorithms was
481 supported by Russian Science Foundation (projects 16-17-10241 and 21-17-00114).
482
483

484

Table 1. Lidar measured aerosol parameters, such as particle depolarization ratios (δ_{355}, δ_{532}, δ_{1064}), lidar ratios (S_{355}, S_{532}), extinction Angstrom exponent ($A^{\alpha}_{355/532}$), fluorescence backscattering coefficient (β_F) and fluorescence capacity (G_F) for several days during March – June 2020 period, when contribution of pollen to the total particle backscattering could be significant.

Day	Height, m	δ_{355}, %	δ_{532}, %	δ_{1064}, %	S_{355}, sr	S_{532}, sr	$A^{\alpha}_{355/532}$	β_F*10^{-4}, Mm^{-1}sr^{-1}	$G_{F*}10^{-4}$
27 Mar	1150	9	12	13	50	42	1.5	2.5	1.2
7 Apr	1150	13	13	13	60	60	1.25	1.0	1.3
8 Apr	1000	11	10	9	50	60	1.0	1.9	1.0
15 Apr	750	15	15	17	40	40	0.7	0.4	0.9
16 Apr	1250	15	15	15	-	-	-	0.6	1.6
19 Apr	650	8	10	14	58	48	1.35	1.2	0.9
20 Apr	1000	18	18	22	55	45	1.2	0.75	1.3
21 Apr	750	15	17	22	66	47	1.25	1.1	1.4
22 Apr	1000	18	18	22	70	55	1.2	0.9	1.5
23 Apr	1000	6	14	11	53	65	1.25	1.5	1.05
30 May	750	7	10	16	-	-	-	0.8	1.2
1 June	750	7	10	16	-	-	-	1.25	1.5

490
491

References

Bohlmann, S., Shang, X., Giannakaki, E., Filioglou, M., Saarto, A., Romakkaniemi, S. and Komppula, M.: Detection and characterization of birch pollen in the atmosphere using multi-wavelength Raman lidar in Finland, Atmos. Chem. Phys. 19, 14559–14569, 2019. doi.org/10.5194/acp-19-14559-2019.

Bohlmann, S., Shang, X., Vakkari, V., Giannakaki, E., Leskinen, A., Lehtinen, K., Pätsi, S., and Komppula, M.: Lidar Depolarization Ratio of Atmospheric Pollen at Multiple Wavelengths, Atmos. Chem. Phys. Discuss., https://doi.org/10.5194/acp-2020-1281.

Cao, X., Roy, G., and Bernier, R.: Lidar polarization discrimination of bioaerosols, Opt. Eng., 49, 116201, https://doi.org/10.1117/1.3505877, 2010.

D'Amato, P.G., Bergmann, K.C., Cecchi, L., Annesi-Maesano, I., Sanduzzi, A., Liccardi, G., Vitale, C., Stanziola, A., D'Amato, M.: Climate change and air pollution: Effects on pollen allergy and other allergic respiratory diseases. Allergo J 23, 32–38, 2014. https://doi.org/10.1007/s15007-014-0484-1

Diehl, K., Quick, C., Matthias-Maser, S., Mitra, S., Jaenicke, R.: The ice nucleating ability of pollen: Part I: Laboratory studies in deposition and condensation freezing modes. Atmospheric Research 58, 75–87, 2001. https://doi.org/10.1088/1748-9326/5/4/044015

Frenguelli, G.: Pollen structure and morphology, Advances in Dermatology and Allergology, 20, 200–204, 2003.

Freudenthaler,V., Esselborn, M.,Wiegner, M.,Heese, B., Tesche, M. and co-authors: Depolarization ratio profiling at severalwavelengths in pure Saharan dust during SAMUM 2006, *Tellus* 61B, 165–179, 2009.

Fröhlich-Nowoisky, J., Kampf, C. J., K., Weber, B., Huffman, J.A., Pöhlker, C., Andreae, M. O., Lang-Yona, N., et al.: Bioaerosols in the Earth system: Climate, health, and ecosystem interactions . Atmospheric Research, 182, 346-76, 2016. https://doi.org/10.1016/j.atmosres.2016.07.018.

Griffiths, P. T., Borlace, J.-S., Gallimore, P. J., Kalberer, M., Herzog, M., and Pope, F. D.: Hygroscopic growth and cloud activation of pollen: a laboratory and modelling study, Atmos. Sci. Lett., 13, 289–295, https://doi.org/10.1002/asl.397, 2012.

Haarig, M., Ansmann, A., Baars, H., Jimenez, C., Veselovskii, I., Engelmann, R., and Althausen, D.: Depolarization and lidar ratios at 355, 532, and 1064 nm and microphysical properties of

523   aged tropospheric and stratospheric Canadian wildfire smoke, Atm. Chem. Phys., 18,
524   11847–11861, 2018.

525   Heidemarie, S. U., Grímsson, F., Weber, M., Zetter, R., Hesse, M., Buchner, R., Svojtka, M., et
526   Frosch-Radivo, A.:. *Illustrated Pollen Terminology*. 2e éd. Springer International
527   Publishing, 2018. http://www.springer.com/gp/book/9783319713649.

528   Hu, Q., Goloub, P., Veselovskii, I., Bravo-Aranda, J.-A., Popovici, I., Podvin, T., Haeffelin, M.,
529   Lopatin, A. , Dubovik, O., Pietras, C., Huang, X., Torres, B., and Chen, C.: Long-range-
530   transported Canadian smoke plumes in the lower stratosphere over northern France, Atmos.
531   Chem. Phys. 19, 1173 – 1193, 2019. doi.org/10.5194/acp-19-1173-2019.

532   Immler, F., Engelbart, D., Schrems, O.: Fluorescence from atmospheric aerosol detected by a
533   lidar indicates biogenic particles in the lower stratosphere, Atmos. Chem. Phys. 5, 345–355,
534   2005.

535   Katifori, E., Alben, S., Cerda, E., Nelson, D. R., and Dumais, J.: Foldable structures and the
536   natural design of pollen grains, P. Natl. Acad. Sci. USA, 107, 7635–7639,
537   https://doi.org/10.1073/pnas.0911223107, 2010.

538   Klett J.D., "Lidar inversion with variable backscatter/extinction ratios", Appl.Opt. 24, 1638-1643,
539   1985.

540   Lake, I.R., Jones, N.R., Agnew, M., Goodess, C.M., Giorgi, F., Hamaoui-Laguel, L., Semenov,
541   M.A., Solomon, F., Storkey, J., Vautard, R., Epstein, M.M.: Climate Change and Future
542   Pollen Allergy in Europe. Environ Health Perspect 125, 385–391, 2017.
543   https://doi.org/10.1289/EHP173

544   Li, B., Chen, S., Zhang, Y., Chen, H., Guo, P.: Fluorescent aerosol observation in the lower
545   atmosphere with an integrated fluorescence-Mie lidar, J. Quant. Spectr. Rad. Transf., 227,
546   211–218, 2019.

547   Mack, S. M., Madl, A. K., Pinkerton, K. E.: Respiratory health effects of exposure to ambient
548   particulate matter and bioaerosols, *Comprehensive Physiology*, 10, 1-20, 2020.
549   https://onlinelibrary.wiley.com/doi/abs/10.1002/cphy.c180040

550   Miyakawa, T., Kanaya, Y., Taketani, F., Tabaru, M., Sugimoto, N., Ozawa, Y., and Takegawa,
551   N.: Ground-based measurement of fluorescent aerosol particles in Tokyo in the spring of 2013:
552   potential impacts of nonbiological materials on autofluorescence measurements of airborne
553   particles, J. Geophys. Res. Atmos., 120, 1171–1185, 2015, doi:10.1002/2014JD022189.

Müller, D., Mattis, I., Wandinger, U., Ansmann, A., Althausen, D., Stohl, A.: Raman lidar observations of aged Siberian and Canadian forest fire smoke in the free troposphere over Germany in 2003: Microphysical particle characterization, J. Geophys. Res., 110, D17201, doi:10.1029/2004JD005756, 2005.

Nicolae D., A. Nemuc, D. Müller, C. Talianu, J. Vasilescu, L. Belegante, and A. Kolgotin: Characterization of fresh and aged biomass burning events using multi-wavelength Raman lidar and mass spectrometry, J. Geophys. Res. 118, 2956–2965, doi:10.1002/jgrd.50324, 2013.

Noh, M. Y., Müller, D., Lee, H., and Choi, T.: Influence of biogenic pollen on optical properties of atmospheric aerosols observed by lidar over Gwangju, South Korea, Atmos. Environ., 69, 139–147, https://doi.org/10.1016/j.atmosenv.2012.12.018, 2013a

Noh, Y. M., Lee, H., Mueller, D., Lee, K., Shin, D., Shin, S., Choi, T. J., Choi, Y. J., and Kim, K. R.: Investigation of the diurnal pattern of the vertical distribution of pollen in the lower troposphere using LIDAR, Atmos. Chem. Phys., 13, 7619–7629, https://doi.org/10.5194/acp-13-7619-2013, 2013b.

Pan, Y.-L.: Detection and characterization of biological and other organic-carbon aerosol particles in atmosphere using fluorescence, J. Quant. Spectr. Radiat. Trans. 150, 12–35, 2015.

Pohlker, C.; Huffman, J.A.; Poschl, U. Autofluorescence of atmospheric bioaerosols-fluorescent biomolecules and potential interferences. Atmos. Meas. Tech. **2012**, 5, 37–71.

Pope, F.D.: Pollen grains are efficient cloud condensation nuclei. Environ. Res. Lett. 5, 044015, 2010. https://doi.org/10.1088/1748-9326/5/4/044015

Rao, Z., He, T., Hua D, Wang, Y., Wang, X., Chen, Y., Le J.: Preliminary measurements of fluorescent aerosol number concentrations using a laser-induced fluorescence lidar, Appl. Opt. 57, 7211-7215, 2018.

Reichardt, J.: Cloud and aerosol spectroscopy with Raman lidar, J. Atm. Ocean. Tech., 31, 1946-1963, 2014.

Reichardt, J., Leinweber, R., Schwebe, A.: Fluorescing aerosols and clouds: investigations of co-existence, Proceedings of the 28th ILRC, Bucharest, Romania, 25-30 June, 2017.

Richardson, S.C., Mytilinaios, M., Foskinis, R., Kyrou, C., Papayannis, A., Pyrri, I., Giannoutsou, E., Adamakis, I.D.S.: Bioaerosol detection over Athens, Greece using the laser

induced fluorescence technique, Science of the Total Environment 696, 133906, 2019. https://doi.org/10.1016/j.scitotenv.2019.133906

Saito, Y., Ichihara, K., Morishita, K., Uchiyama, K., Kobayashi, F., Tomida, T.: Remote detection of the fluorescence spectrum of natural pollens floating in the atmosphere using a laser-induced-fluorescence spectrum (LIFS) lidar, Remote Sens., 10, 1533, 2018. doi:10.3390/rs10101533.

Sassen, K.: Boreal tree pollen sensed by polarization lidar: Depolarizing biogenic chaff, Geophys. Res. Lett., 35, L18810, https://doi.org/10.1029/2008GL035085, 2008.

Sassen, K.: Elliptical pollen corona from North American boreal paper birch trees (Betula papyrifera): strong fall orientations for near-spherical particles, Appl. Opt., 50, F1–F5, https://doi.org/10.1364/AO.50.0000F1, 2011.

Shang, X., Giannakaki, E., Bohlmann, S., Filioglou, M., Saarto, A., Ruuskanen, A., Leskinen, A., Romakkaniemi, S., Komppula, M.: Airborne pollen observations using a multi-wavelength Raman polarization lidar in Finland: characterization of pure pollen types, Atm. Chem. Phys., 20, 15323–15339, 2020. doi.org/10.5194/acp-20-15323-2020.

Sofiev, M., Vira, J., Kouznetsov, R., Prank, M., Soares, J., Genikhovich, E.: Construction of the SILAM Eulerian atmospheric dispersion model based on the advection algorithm of Michael Galperin. Geoscientific Model Development 8, 3497–3522, 2015. https://doi.org/10.5194/gmd-8-3497-2015

Sicard, M., Izquierdo, R., Alarcón, M., Belmonte, J., Comerón, A., and Baldasano, J. M.: Near-surface and columnar measurements with a micro pulse lidar of atmospheric pollen in Barcelona, Spain, Atmos. Chem. Phys., 16, 6805–6821, https://doi.org/10.5194/acp-16-6805-2016, 2016.

Stein, A.F., Draxler, R.R, Rolph, G.D., Stunder, B.J.B., Cohen, M.D., and Ngan, F.: NOAA's HYSPLIT atmospheric transport and dispersion modeling system, Bull. Amer. Meteor. Soc., 96, 2059-2077, 2015. http://dx.doi.org/10.1175/BAMS-D-14-00110.1

Steiner, A. L., Brooks, S. D., Deng, C., Thornton, D. C.O., Pendleton, M. W., Bryant, V:. Pollen as atmospheric cloud condensation nuclei, *Geophysical Research Letters*, 2015GL064060, 2015. https://doi.org/10.1002/2015GL064060.

Sugimoto, N. and Lee, C. H.: Characteristics of dust aerosols inferred from lidar depolarization measurements at two wavelength, Appl. Opt., 45, 7468–7474, 2006.

615 Sugimoto, N., Huang, Z., Nishizawa, T., Matsui, I., Tatarov, B.: Fluorescence from atmospheric
616   aerosols observed with a multichannel lidar spectrometer," Opt. Expr. 20, 20800-20807,
617   2012.

618 Tesche, M., Ansmann, A., Müller, D., Althausen, D., Engelmann, R., Freudenthaler, V., and
619   Groß, S.: Vertically resolved separation of dust and smoke over Cape Verde using
620   multiwavelength Raman and polarization lidars during Saharan Mineral Dust Experiment
621   2008, J. Geophys. Res., 114, D13202, doi:10.1029/2009JD011862, 2009.

622 Veselovskii, I., Whiteman, D. N., Korenskiy, M., Suvorina, A., Kolgotin, A., Lyapustin, A.,
623   Wang, Y., Chin, M., Bian, H. Kucsera, T. L., Perez-Ramirez, D., Holben, B.:
624   Characterization of forest fire smoke event near Washington, D.C. in Summer 2013 with
625   multi-wavelength lidar. Atmos. Chem. Phys. 15, 1647–1660, 2015.

626 Veselovskii, I., Hu, Q., Goloub, P., Podvin, T., Korenskiy, M., Pujol, O., Dubovik, O., Lopatin,
627   A.: Combined use of Mie-Raman and fluorescence lidar observations for improving aerosol
628   characterization: feasibility experiment, Atm. Meas. Tech., 13, 6691–6701, 2020.
629   doi.org/10.5194/amt-13-6691-2020a.

630 Veselovskii, I., Hu, Q., Goloub, P., Podvin, T., Korenskiy, M., Derimian, E., Legrand, M.,
631   Castellanos, P.: Variability of Lidar-Derived Particle Properties Over West Africa Due to
632   Changes in Absorption: Towards an Understanding. Atm. Chem. Phys., 20, 6563-6581,
633   2020b. doi.org/10.5194/acp-20-6563-2020

634

635

Figures
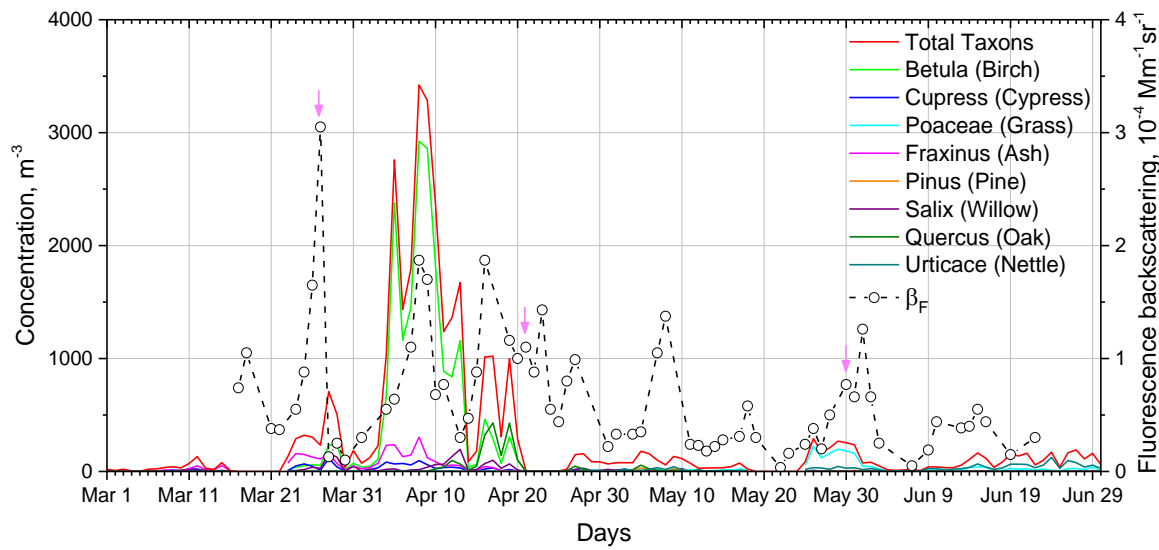
638   Fig.1. Daily concentration of most abundant pollen taxa, for the period March–June 2020 in Lille

639   from in situ measurements on the rooftop. Open symbols show fluorescence backscattering β_F

640   measured by lidar. Lidar measurements are averaged over night and maximal value in 500–1000

641   m range is shown. Vertical arrows mark the sessions, which are further analyzed in Fig.8, 10, 11.

642

643

644

645

646
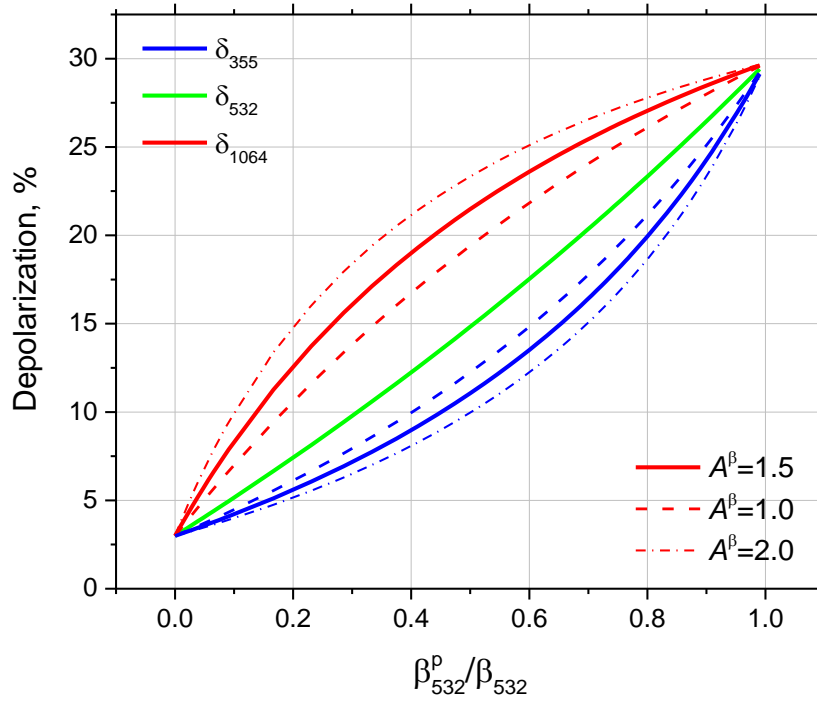
647 Fig.2. Depolarization ratios at 355, 532 and 1064 nm as a function of pollen contribution to the

648 total backscattering coefficient $\dfrac{\beta_{532}^{p}}{\beta_{532}}$. Depolarization ratios of pollen (δ^{p}) and background aerosol

649 (δ^{b}) are assumed to be spectrally independent δ^{p}=30% and δ^{b}=3%. Backscattering coefficient of

650 pollen is spectrally independent. The backscattering Angstrom exponents of background aerosol

651 were assumed to be the same for both pairs of wavelengths ($A_{355/532}^{\beta} = A_{532/1064}^{\beta}$), and results are

652 shown for the values A^{β}=1.0, 1.5, 2.0.

653

654

655

656
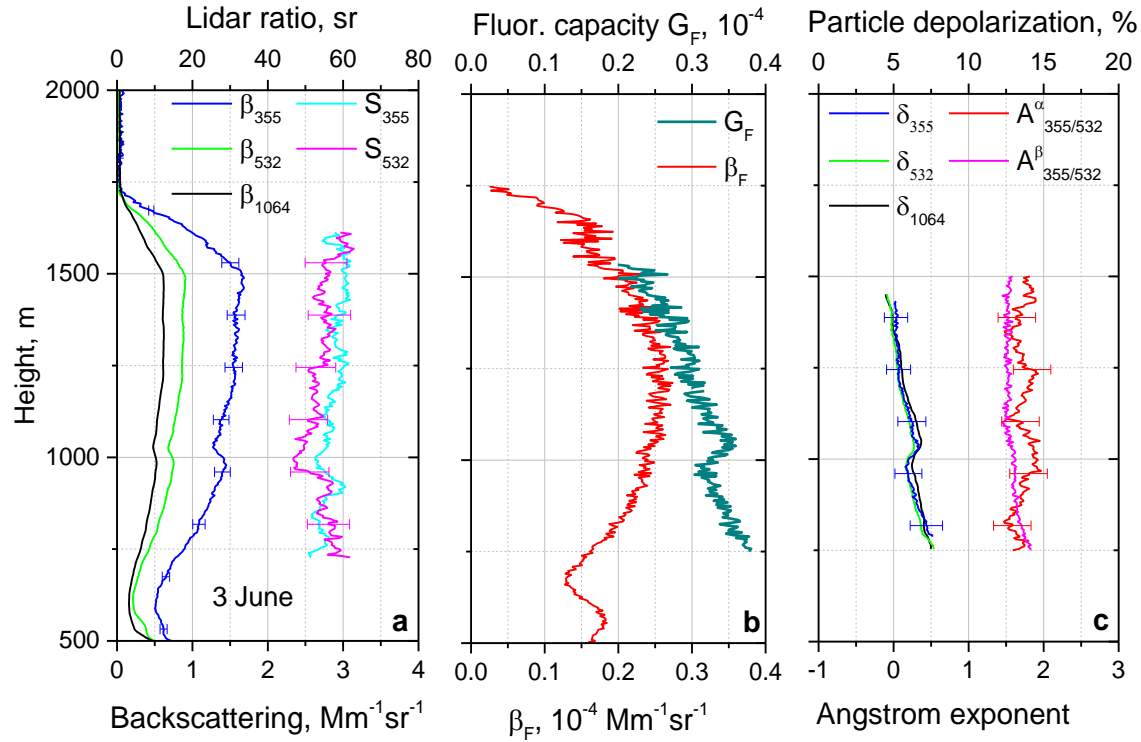
657 Fig.3. Measurements in the condition of background aerosol predominance. Vertical profiles of

658 (a) backscattering coefficients β_{355}, β_{532}, β_{1064} and lidar ratios S_{355}, S_{532}; (b) fluorescence

659 backscattering β_F and fluorescence capacity $G_F = \beta_F/\beta_{532}$; (c) particle linear depolarization ratios

660 δ_{355}, δ_{532}, δ_{1064} together with extinction and backscattering Angstrom exponents $A^{\alpha}_{355/532}$, $A^{\beta}_{355/532}$

661 on 3 June 2020 for 20:30 – 23:00 UTC. Measurements were performed at 30 degree to the

662 horizon.

663

664

665

666

667

668

669

670
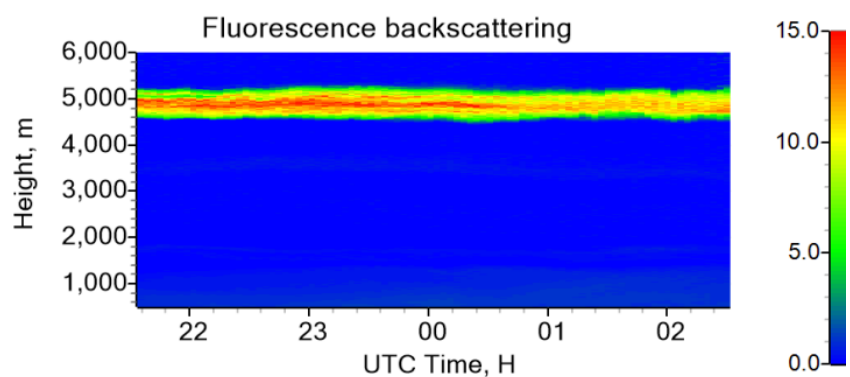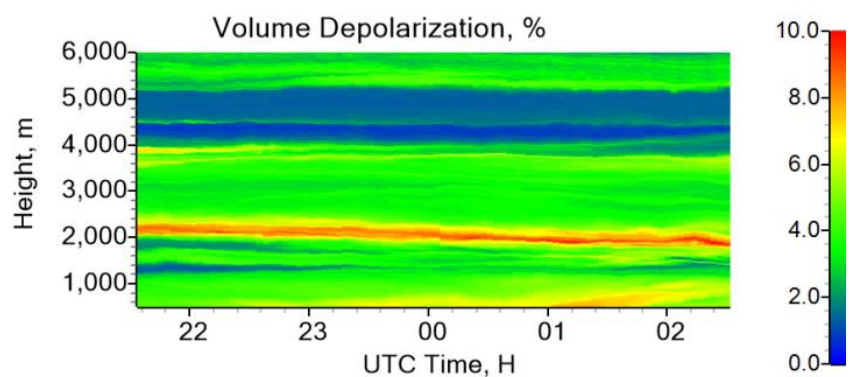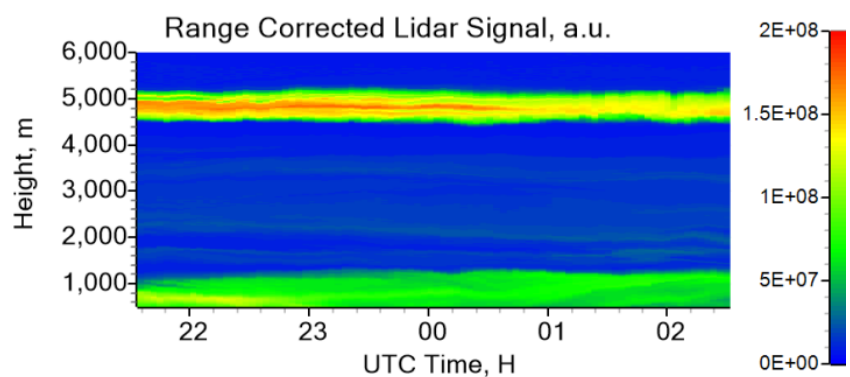
Fig.4. Range corrected lidar signal at 1064 nm, volume depolarization ratio at 1064 nm and fluorescence backscattering coefficient (in 10^{-4} $Mm^{-1}sr^{-1}$) on 23-24 June 2020.

673

674

675

676
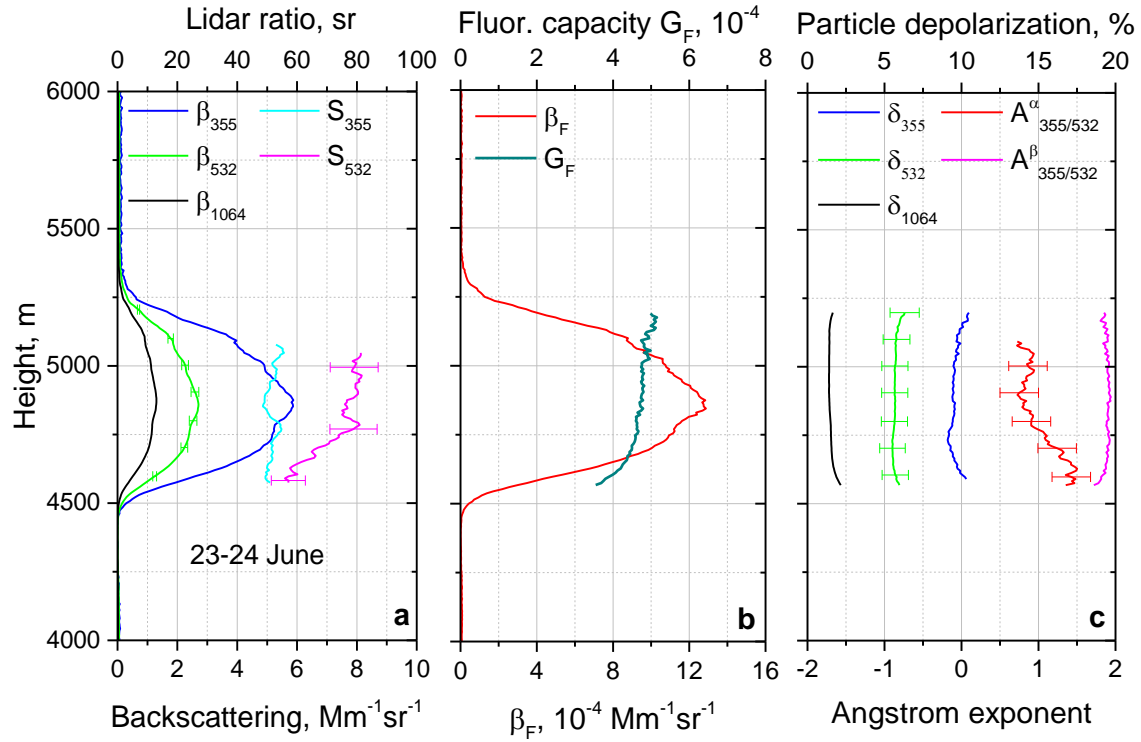
Fig.5. Vertical profiles of (a) backscattering coefficients β_{355}, β_{532}, β_{1064}, lidar ratios S_{355}, S_{532}; (b) fluorescence backscattering coefficient β_F, fluorescence capacity G_F; and (c) particle depolarization ratios δ_{355}, δ_{532}, δ_{1064} together with the extinction and backscattering Angstrom exponents $A^{\alpha}_{355/532}$, $A^{\beta}_{355/532}$ on the night 23-24 June 2020 for 21:30 – 02:30 UTC.

681

682

683
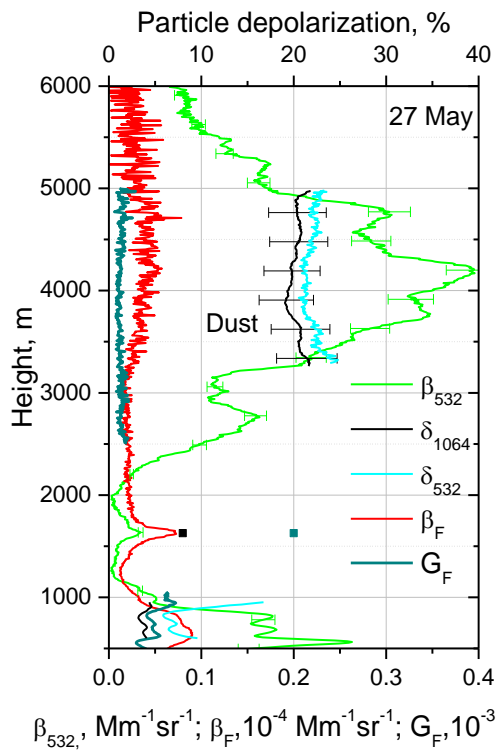
684

685   Fig.6. Lidar measurements during dust episode. Vertical profiles of particle β_{1064} and

686   fluorescence β_F backscattering coefficients, fluorescence capacity G_F and particle depolarization

687   ratios δ_{1064}, δ_{532} on 27 May 2020 for 21:00–23:00 UTC.

688

689

690

691

692
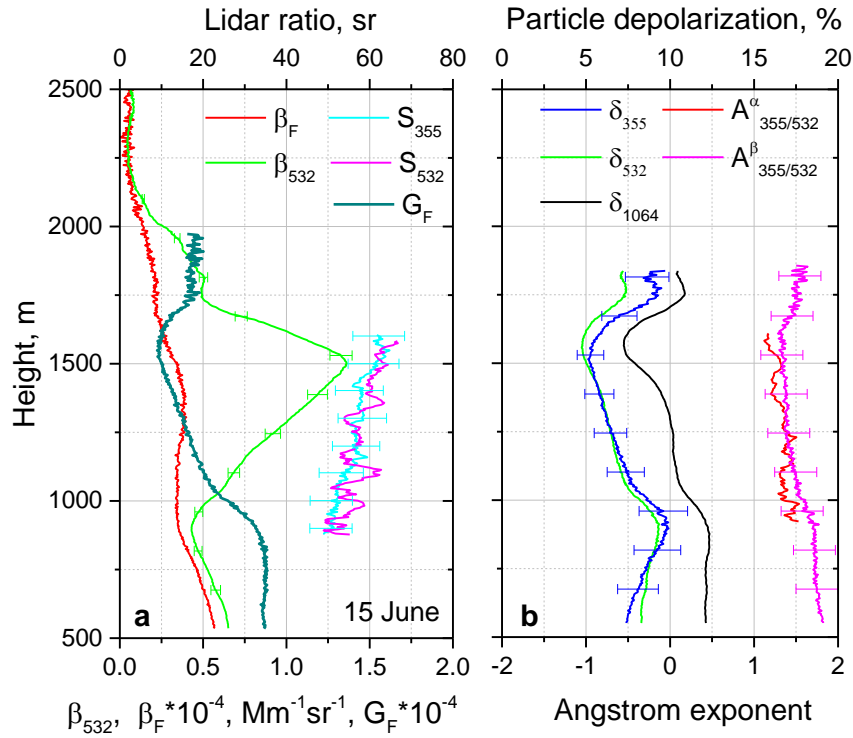
Fig.7. Lidar measurements in the condition of the aerosol hygroscopic growth in 900-1500 m height range. Vertical profiles of (a) particle β_{532} and fluorescence β_F backscattering coefficients, fluorescence capacity G_F, lidar ratios S_{355}, S_{532} and (b) particle depolarization ratios δ_{355}, δ_{532}, δ_{1064} together with extinction $A^{\alpha}_{355/532}$ and backscattering $A^{\beta}_{355/532}$ Angstrom exponents measured on 15 June 2020 for 22:00 – 24:00 UTC.

698

699

700

701
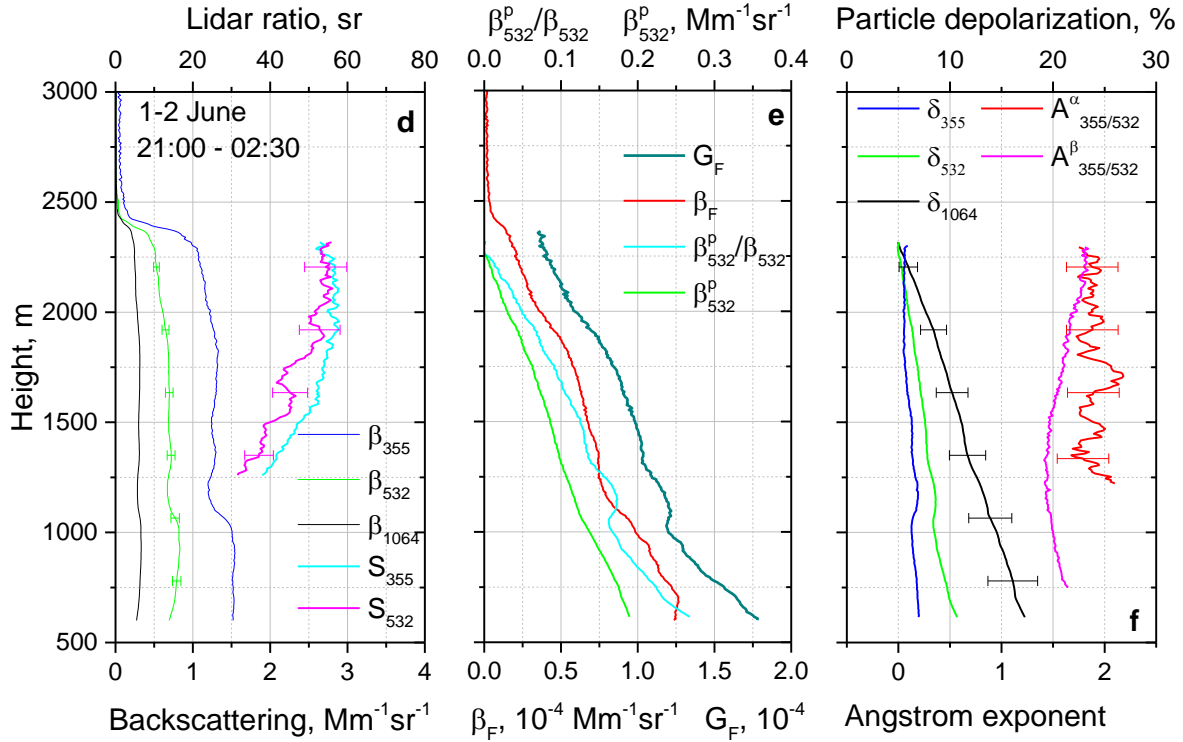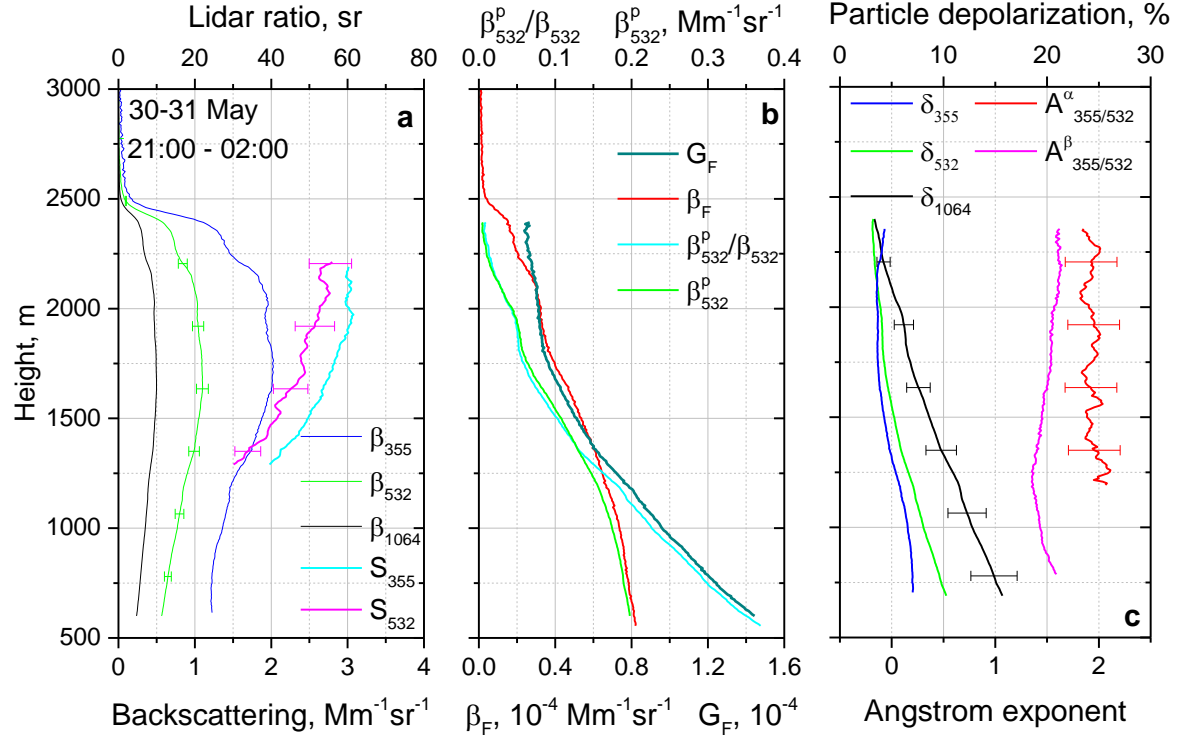
Fig.8. Vertical profiles of (a, d) particle backscattering coefficients β_{355}, β_{532}, β_{1064} and lidar ratios S_{355}, S_{532}, (b, e) fluorescence backscattering coefficient β_F, fluorescence capacity G_F,

704   pollen backscattering coefficient β_{532}^p and its contribution to the total backscattering $\dfrac{\beta_{532}^p}{\beta_{532}}$; (c, f)

705   particle depolarization ratios δ_{355}, δ_{532}, δ_{1064} together with extinction $A_{355/532}^\alpha$ and backscattering

706      $A_{355/532}^\beta$ Angstrom exponents on (a-c) 30 - 31 May 2020 for 21:00 – 02:00 UTC and on (d-f) 1-2

707   June 2020 for 21:00 – 02:30 UTC. Profiles of β_{532}^p and $\dfrac{\beta_{532}^p}{\beta_{532}}$ were computed in assumption of

708      $\delta_{532}^p = 30\%$. The depolarization ratios of the background aerosol δ_{532}^b are measured/assumed to

709   be 3% on 30 May and 5% on 1 May.

710

711

712

713

714

715

716

717

718

719

720

721

722

723

724

725

726

727
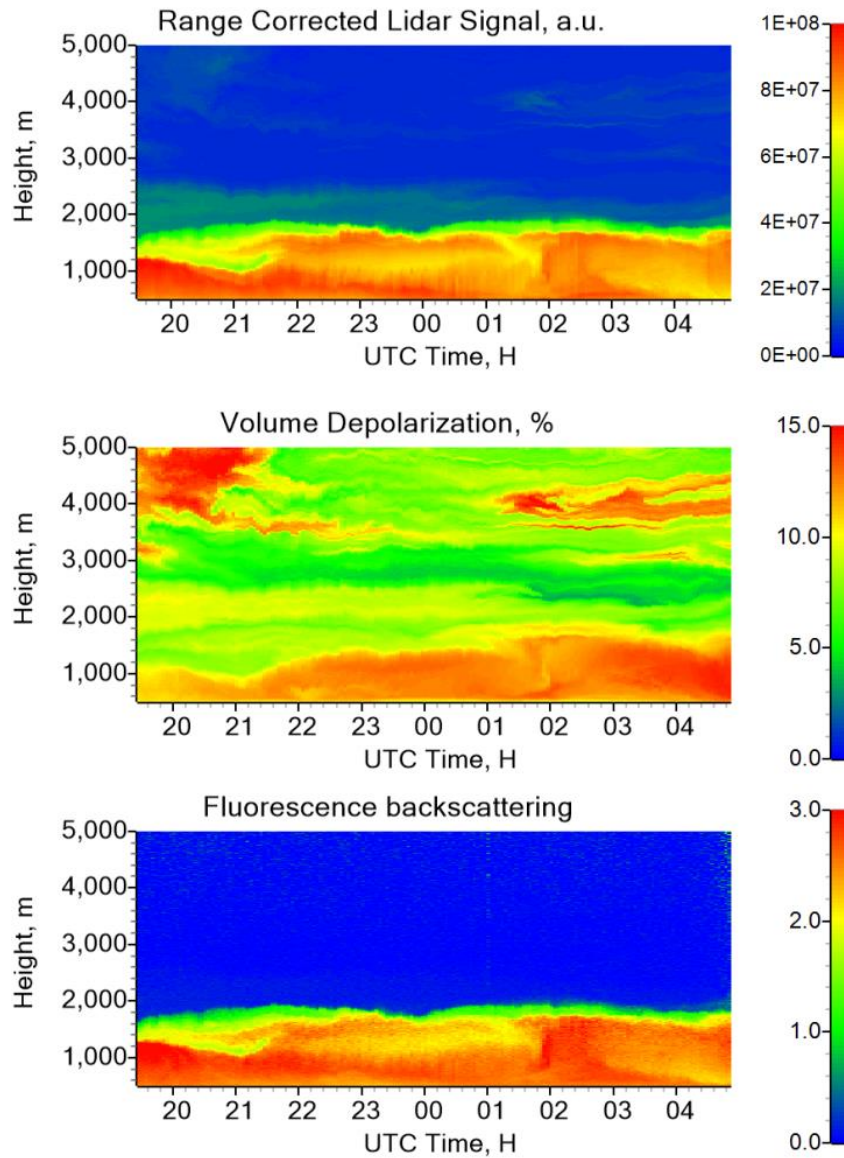
728 Fig.9. Range corrected lidar signal at 1064 nm (upper panel), volume depolarization ratio at 1064

729 nm (middle panel) and fluorescence backscattering coefficient (in 10^{-4} $Mm^{-1}sr^{-1}$, lower panel)

730 measured on 27-28 March 2020.

731

732
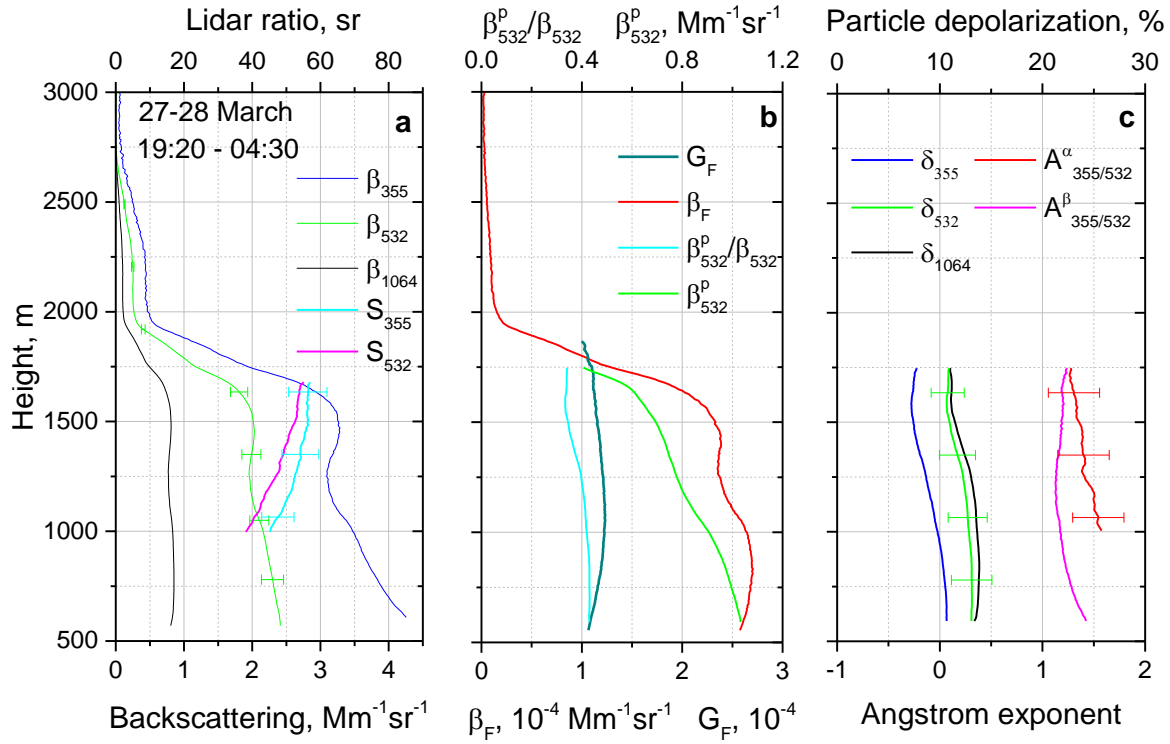
733

734 Fig.10. Vertical profiles of (a) particle backscattering coefficients β_{355}, β_{532}, β_{1064} and lidar ratios

735 S_{355}, S_{532}; (b) fluorescence backscattering coefficient β_F, fluorescence capacity G_F, pollen

736 backscattering coefficient β_{532}^p and its contribution to the total backscattering $\dfrac{\beta_{532}^p}{\beta_{532}}$; (c) particle

737 depolarization ratios δ_{355}, δ_{532}, δ_{1064} together with extinction $A_{355/532}^\alpha$ and backscattering $A_{355/532}^\beta$

738 Angstrom exponents measured on 27 - 28 March 2020 for19:20 – 04:30 UTC. Profiles of β_{532}^p

739 and $\dfrac{\beta_{532}^p}{\beta_{532}}$ were computed in assumption of $\delta_{532}^p = 30\%$ and $\delta_{532}^b = 3\%$.

740

741
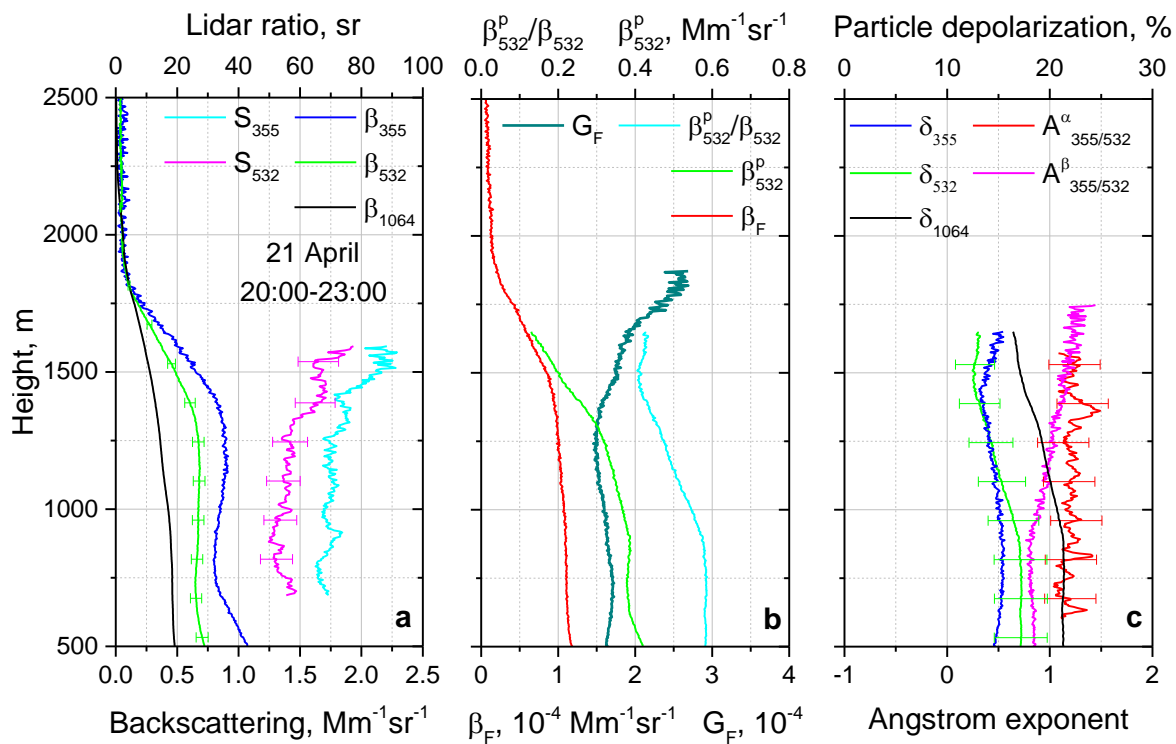
742

743 Fig.11. The same particle parameters as in Fig.10 for 21 April 2020, 20:00-23:00 UTC.
744 Measurements were performed at 30 deg to horizon.
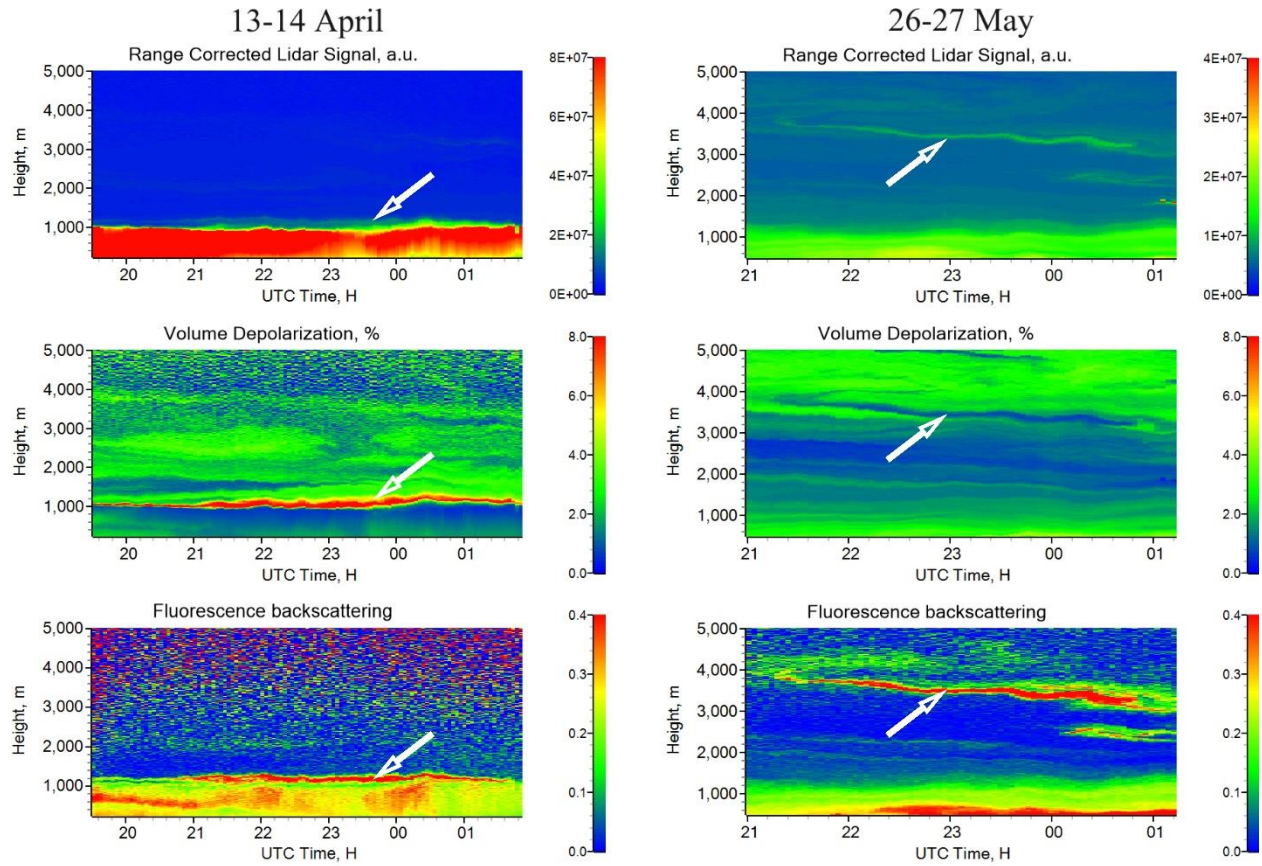
Fig.12. Range corrected lidar signal at 1064 nm, volume depolarization ratio δ_{1064}^{v} and fluorescence backscattering coefficient (in 10^{-4} $Mm^{-1}sr^{-1}$) measured on 13-14 April (left column) and 26-27 May 2020 (right column). Arrows point to the fluorescent layers.

751

752
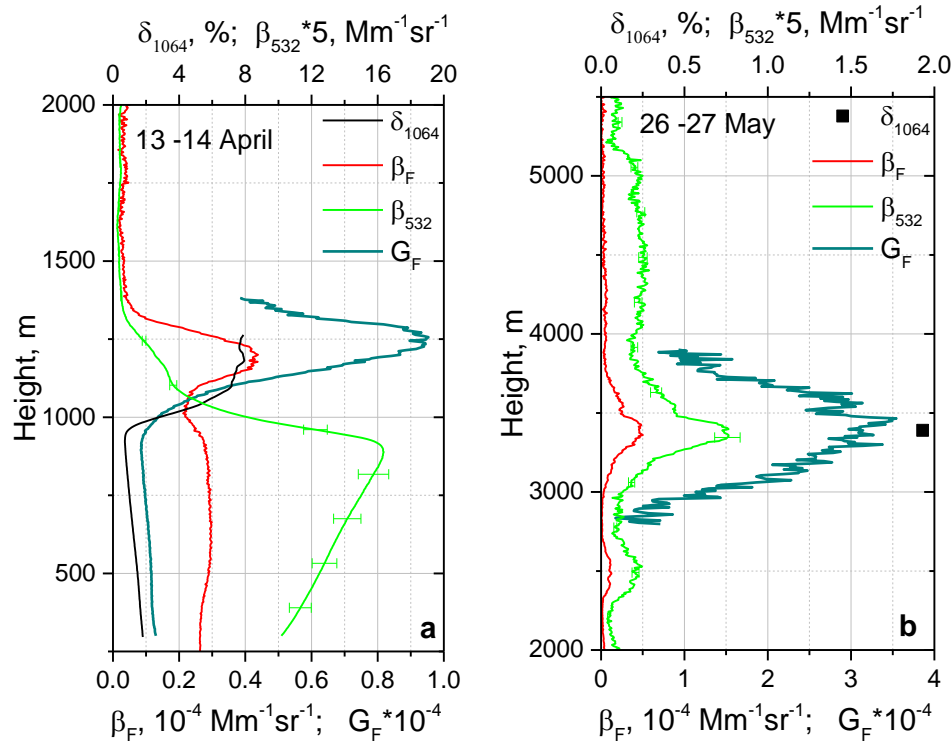
Fig.13. Vertical profiles of elastic β_{532} and fluorescence β_F backscattering coefficients, fluorescence capacity G_F and particle depolarization ratio δ_{1064} measured on (a) 13-14 April for 21:00 – 01:00 UTC and (b) 26-27 May 2020 for 23:30 – 00:40 UTC. Values of β_{532} are multiplied by factor 5.

757

758

759

760

761
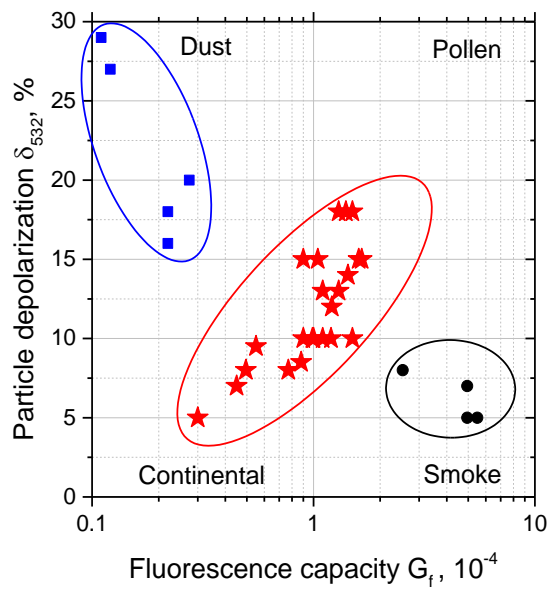
Fig.14. Particle depolarization δ_{532} versus fluorescence capacity G_F. This diagram allows to identify dust (blue), smoke particles (black) and aerosol mixtures containing pollen (red).

764

765